Chapter 7
Electromagnetic Effects of IR-UWB Implant Communication

Abstract With the increased use of Impulse Radio-Ultra-Wideband (IR-UWB) devices within or at close proximity to the human body, it is of utmost importance to analyze the electromagnetic effects caused by those devices. As human tissue is exposed to the electromagnetic signals emitted from IR-UWB devices, they absorb a certain amount of transmitted power and convert it into heat. This phenomenon causes a temperature increase in the human tissue. The heating effect of the human tissue is significant for high-frequency and high-bandwidth signals, such as the IR-UWB signals. The temperature increase of the tissue material should be regulated in order to prevent any adverse effects caused by the exposure to electromagnetic signals. Specific Absorption Rate (SAR) and Specific Absorption (SA) provide a good indication of the amount of power absorbed by the himan tissues. This chapter presents the SAR, SA and temperature variation of the human body caused by IR-UWB signals. An IR-UWB based Wireless Capsule Endoscopy (WCE) that operates inside the human abdomen is used as the main application for this study. This analysis compares the compliance of the IR-UWB based WCE devices with international safety regulations. A voxel model of the human body consisting of human tissue simulating materials is used for this simulation-based study. The tissue properties, such as relative permittivity, are characterized according to the incident signal frequency and age of the tissue sample during simulations. The SAR and SA variations are analyzed using the Finite Integration Technique (FIT) as the discretization model.

Keywords SAR/SA · Wireless capsule endoscopy · Head implant · Electromagnetic effects · Temperature increase · Bio-heat equation · IR-UWB

7.1 Introduction

Wireless communication for implantable sensor devices has drawn the attention of researchers in recent years due to the several advantages it possesses, such as minimizing restrictions in daily activities, facilitating less invasive surgical

K. M. S. Thotahewa et al., *Ultra Wideband Wireless Body Area Networks*,
DOI: 10.1007/978-3-319-05287-8_7,

procedures and offering remote control and monitoring [1–4]. With the extensive use of wireless devices within or at close proximity to the human body, electromagnetic effects caused by the interaction between radio frequency waves and human tissues are of paramount importance. SAR, which determines the amount of signal energy absorbed by the human body tissue, is used as the index for many standards to regulate the amount of exposure of the human body to electromagnetic radiation [5, 6]. Various regulatory bodies provide different assessment methods and different maximum allowable SAR limits for the human tissue that are exposed to electromagnetic signals. Regulations by the International Council on Non-Ionizing Radiation Protection (ICNIRP) standard limit the localized 10 g averaged SAR in the head to 2 W/kg for signals in the range of 10 kHz to 10 GHz [5]. The IEEE/ICES C95.1-2005 standard limits the 10 g averaged SAR value over a six minute time period to 1.6 W/kg [6]. Additional regulations are applied for pulsed transmission schemes in order to prevent auditory effects. A 2 mJ/kg SA averaged over 10 g tissue weight for a single pulse is applied by the ICNIRP standard while 576 J/kg averaged over a 10 g tissue for a six minute period is applied by the IEEE/ICES C95.1-2005 standard. Some of the international standards that provide regulations on SAR limits are depicted in Table 7.1.

Studies have shown that a temperature increase in excess of 1 °C can prove harmful to the human body [5]. Many studies have been carried out in order to assess the effect of radio frequency signals [7–15]. Most of the research work in this area has been done based on on-body scenarios, where most of the signal propagation occurs through air interface before coming into contact with the body tissues [10–15]. Because of the increased use of implantable wireless devices, where most of the electromagnetic wave propagation occurs within the human tissue, it is important to analyze the effects of those devices on the human body. Only a few studies found in the literature investigate the effects of in-body propagation of electromagnetic waves on human tissue [7, 8]. With the emergence of new techniques to record physiological data such as neural recording systems [16, 17] and WCE [18], the need for high data rate wireless transmission has become a key requirement for implantable devices. Impulse Radio Ultra Wide Band (IR-UWB) can be identified as a technology that caters the need for high data rate while requiring low power consumption.

As UWB communication becomes more prominent in high data rate implant communication [16–18, 20, 21], it is important to investigate the electromagnetic effects caused by a UWB transmitter implanted in the human body. Several publications are found in the literature that have analysed the effect of UWB on the human body based on on-body scenarios [12–15]. They investigate the SAR variation caused by a UWB transmitting source placed externally at a close proximity of the human body. These results provide a general understanding about the electromagnetic effects caused by on-body propagation of UWB signals. Many reported studies used homogeneous human body models without considering the differences in properties of various types of tissue materials, which can significantly affect the results. SAR variation also depends on antenna properties, such as directivity, orientation and gain. A few reported studies demonstrate the effects of

Table. 7.1 Electromagnetic exposure limits provided by various regulatory bodies [19]

	Standard	Averaging method	Freq. range	Whole body avg. SAR (W kg^{-1})	Localised SAR (head and trunk) (W kg^{-1})	Limbs (W kg^{-1})
Occupational exposure/ controlled environment	ICNIRP 2009	Averaged over cross section of 1 cm^2 perpendicular to current direction and for 6 min period	100 kHz–10 GHz	0.4	10	20
	IEEE/ICES C95.1-2005	Averaged over 10 g tissue for 6 min	100 kHz–3 GHz	0.4	10	20
	Health Canada Safety Code 6 2009	Tissue volume in form of cube and averaged over 6 min period	100 kHz–6 GHz	0.4	8	20
	CENELEC 1995	Averaged over 10 g tissue for 6 min	10 kHz–30 GHz	0.4	10	20
General public exposure/ controlled environment	ICNIRP 2009	Averaged over cross section of 1 cm^2 perpendicular to current direction and for 6 min period	100 kHz–10 GHz	0.08	2	4
	IEEE/ICES C95.1-2005	Averaged over 10 g tissue in a cube and averaged over 30 min period	100 kHz–3 GHz	2	2	4
	Health Canada Safety Code 6 2009	Tissue volume in form of cube	100 kHz–6 GHz	0.08	1.6	4
	CENELEC 1995	Averaged over 10 g tissue for 6 min	10 kHz–30 GHz	0.08	2	4

radio frequency transmission from implantable devices inside the human body [7, 8, 22]. Some of them report the SAR variations caused by implantable devices operating at low frequency bands such as MICS and ISM bands [7, 8]. The work reported in [22] illustrates the SAR variation caused by an IR-UWB source inside the human stomach. The latter uses the Finite Difference Time Domain (FDTD) computation method, which discretises the derivatives in Maxwell's curl equations [23] using finite differences. However, [22] has not considered an antenna model in the simulations; additionally, the FCC regulations that govern the UWB indoor propagation are not taken into account. Many studies have analysed path-loss as the sole indicator of electromagnetic power absorption [24–27]. However, SAR and SA measurements can be associated easily with the temperature increase in the human tissue.

This chapter presents the electromagnetic effects and thermal effects of IR-UWB implant communication, which are important safety measures in the applications of body area network applications. IR-UWB based WCE is used as the application of focus in this chapter. A human anatomical body model developed by CST Studio [28], which has been recognised by the Federal Communications Commission (FCC) [29] as a suitable simulation tool for SAR calculations, is used to simulate the human tissue properties at UWB frequencies. An implantable antenna working at UWB frequencies is used as the source of the UWB signals. The 4-Cole Cole model [30] is used in order to consider the dispersive nature of the tissue materials at these high frequencies. In addition, the effect of the human age is considered when calculating the tissue properties such as relative permittivity. An IR-UWB pulse operating at a centre frequency of 4 GHz and a bandwidth of 1 GHz has been chosen as the excitation to the antenna. This range is selected so that the UWB spectrum has minimum interference from other wireless technologies, such as 5 GHz Wi-Fi.

7.2 Simulation Models and Methods

This section givens a brief introduction to the simulation models and methods used for calculation of SAR and temperature increase of human tissue that is exposed to IR-UWB signals.

7.2.1 Effect of Human Tissue Properties on SAR

A compilation of experimental and theoretical results on human tissue property variation depending on the incident frequency provided in [30, 31] proves that the former behaves differently at different incident frequencies. This is due to a property known as dielectric dispersion. The SAR value for a certain material subjected to an electromagnetic field can be calculated by (7.1) [32].

$$\mathrm{SAR} = \frac{1}{2}\frac{\sigma}{\rho}|\mathrm{E}|^2 \tag{7.1}$$

where E is the root mean square (RMS) electric field strength, ρ is the mass density (in kg/m^3), and σ is the conductivity of the tissue. The electric field and the magnetic field in the frequency domain can be described by Maxwell's curl equations in the frequency domain as below:

$$\nabla \times \boldsymbol{E}(\boldsymbol{\omega}) = -j\omega\mu\boldsymbol{H}(\boldsymbol{\omega}) \tag{7.2}$$

$$\nabla \times \boldsymbol{H}(\boldsymbol{\omega}) = j\omega\varepsilon_0\varepsilon_r'(\omega)\boldsymbol{E}(\boldsymbol{\omega}) \tag{7.3}$$

where $\mathrm{j} = \sqrt{-1}$ is the imaginary unit, ω is the angular frequency, $\boldsymbol{E}(\boldsymbol{\omega})$ and $\boldsymbol{H}(\boldsymbol{\omega})$ are time-harmonic electric and magnetic fields, μ is the permeability, ε_0 is the free space permittivity and $\varepsilon_r'(\omega)$ is the frequency dependent complex relative permittivity. Because of the dependency of the electric field on$\varepsilon_r'(\omega)$, the SAR variation inherently depends on the relative permittivity of the material, which itself depends on the incident frequency of the electromagnetic signal. The behavior of the complex relative permittivity for different tissue types differs from each other, especially at higher frequency ranges such as UWB. Hence, it is not advised to use straightforward homogeneous body models to simulate the electromagnetic effects at higher frequencies. The simulations presented in this chapter use the CST Studio voxel human model, which is a human body model consisting of a mixture of tissue materials such as brain, bone, intestinal tissue, colon tissue, fat and skin. It also considers blood flow for thermal calculations.

The frequency dependent dielectric permittivity of human tissue can be expressed as [33]:

$$\varepsilon_r'(\omega) = \varepsilon' - j\varepsilon'' = \varepsilon' - j\frac{\sigma}{\varepsilon_0\omega} = \varepsilon'\left(1 - j\frac{1}{\omega\tau}\right) \tag{7.4}$$

where ε' is the relative permittivity of the tissue material, ε'' is the out of phase loss factor, which can be expressed as $\varepsilon' = \frac{\sigma}{\varepsilon_0\omega}$ and $\tau = \frac{\varepsilon_0\varepsilon'}{\sigma}$ is the relaxation time constant. In the expression for ε'', σ represents the total conductivity of the material, which might be partially attributed by frequency dependent ionic conductivity σ_i, $\varepsilon_0 = 8.85 \times 10^{-12}$ F/m is the permittivity of the free space and ω is the angular frequency. Based on this equation, Gabriel et al. have proposed a method of evaluating the frequency dependent relative permittivity of a material by so-called 4-Cole Cole model approximation given in the equation below [30]:

$$\varepsilon_r'(\omega) = \varepsilon_\infty + \sum_{n=1}^{4}\frac{\Delta\varepsilon_n}{1 + (j\omega\tau_n)^{1-\alpha_n}} + \frac{\sigma_i}{j\omega\varepsilon_0} \tag{7.5}$$

where ε_∞ is the permittivity when $\omega \to \infty$ (permittivity in Terahertz frequencies in practical scenarios), $\Delta\varepsilon_n$ is the change in the permittivity in a specified frequency range during nth iteration, τ_n is the relaxation time during the nth iteration, α_n is the nth iteration of the distribution parameter which is a measure of the broadening of dispersion and σ_i is the static ionic conductivity. Due to the high computational complexity involved when calculating the SAR in the time domain, for example when using the FDTD method, most of the literature available for SAR variation in body tissues used an approximation method such as the Debye approximation [9] or the so called 4 × L Cole Cole approximation [22] instead of the more accurate 4-Cole Cole model of tissue properties. This is mainly due to the fact that obtaining a time domain expression for $\varepsilon_r'(\omega)$ for $0 < \alpha_n < 1$ is computationally intensive. The approach followed in this chapter has been to compute the SAR in the frequency domain, which enables to use the more accurate 4-Cole Cole approximation in the obtained calculations.

Apart from the frequency dependent dispersive nature of the tissue materials, the human age affects the electromagnetic behavior of body tissues. This is mainly due to the change in the water content of tissue with age [34, 35]. Methods presented in [36] follow the Lichtenecker's exponential law for the complex permittivity based on the water content of the human tissue materials [37]. According to the information given in [37], the relative permittivity of any tissue material (i.e. real part of the complex relative permittivity (ε' in (7.4)) can be calculated as:

$$\varepsilon' = \varepsilon_w^{\beta} \varepsilon_t^{1-\beta} \tag{7.6}$$

where ε_W is the permittivity of water, ε_t is the age independent relative permittivity of the tissue organic material and β is the hydrate rate for the tissue material. β can be expressed as $\beta = \rho \cdot TBW$, where $TBW = 784 - 241 \cdot e^{\left\{-\left[\frac{\ln\left(\frac{AGE}{55}\right)}{6.9589}\right]^2\right\}}$ is the total body water index ("AGE" is the age of the tissues sample in years) [36, 38]. After some primary operations, the frequency dependent complex permittivity for body tissues can be expressed as follows [36]:

$$\varepsilon_r'(\omega) = \varepsilon_w^{\frac{\beta-\beta_A}{1-\beta_A}} \varepsilon_A^{\frac{1-\beta}{1-\beta_A}} \left(1 - j\frac{1}{\omega\tau}\right) \tag{7.7}$$

where ε_A is the age dependent relative permittivity of a reference adult tissue material which can be expressed as $\varepsilon_A = \varepsilon_w^{\beta_A} \varepsilon_t^{1-\beta_A}$ by replacing $\varepsilon' = \varepsilon_A$ in (7.6) (for present simulations, the tissue parameters of a 55 year old adult are used as reference) and β_A is the hydrate rate for adult tissues (all other parameters are described in (7.4) and (7.6)). By using the 4-Cole Cole approximation in combination with the age related tissue parameter approximations it is possible to characterize the human tissue properties with sufficient precision. This approach has been utilized in the present study. This study also considers the relative

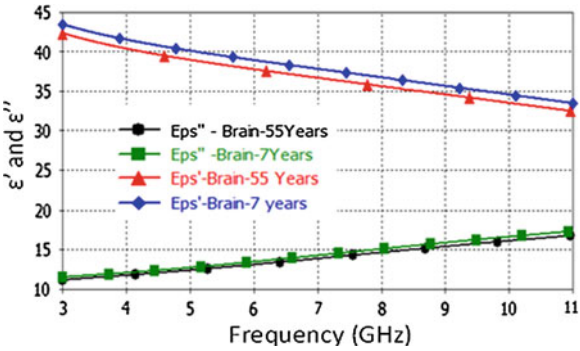

Fig. 7.1 Simulated variation of ε' and ε'' in the UWB frequency range, IEEE copyright [39]

permittivity variation of water depending on the incident frequency instead of the constant value used in [36] for age related calculations. Figure 7.1 depicts an example for the variation of ε' and ε'' as a function of frequency for the brain tissue material of a child of 7 years and a male of 55 years [39]. The basic set of tissue parameters required for the calculation (e.g. $\tau_1 - \tau_4$, $\Delta\varepsilon_1 - \Delta\varepsilon_4$ and $\alpha_1 - \alpha_4$) of the 4-Cole Cole approximation is taken from [33]. It should be observed that while ε' depends on the variation of the tissue water content with age, ε'' is largely age independent as the latter is determined by the conductivity (σ). This can be seen in Fig. 7.1.

7.2.2 SAR Calculation Method

The Finite Integration Technique (FIT) is used as the volume discretization approach for the described simulations. This technique is used to calculate the absorption loss of the body tissues by discretising the Maxwell's curl equations in a specified domain. The discretising volume element is chosen to be cubic, and appropriate boundary conditions are applied in order to define the power absorbed within that cube. Further information on the FIT model can be found in [40, 41].

SAR is defined as the power absorbed by the mass contained within that discretised volume element as shown in (7.8) [42].

$$SAR = \frac{d\left(\frac{\Delta W}{\rho dV}\right)}{dt} \tag{7.8}$$

where ΔW is the power absorbed by the discretised volume element, ρ is the density of the human tissue material, dt is the incremental time and dV is its incremental volume. Present simulations use an IR-UWB signal pulse as the excitation signal, and are conducted in order to calculate the 10 g averaged SAR so as to compare it with the ICNIRP specifications for pulse transmission [5]. The maximum SAR within the 10 g of tissue averaging volume is taken into

consideration in order to demonstrate the worst-case scenario. The Specific Absorption (SA) per pulse, which is being used to introduce additional limitations for pulsed transmissions in the ICNIRP limitations, is computed using:

$$SA = SAR \times T_p \tag{7.9}$$

where T_p is the pulse duration.

It should be noted that heat sources such as the electronic components used in the implanted circuitry also affect the SAR variation in the body tissues. The influence of these heat sources are not considered in the performed simulations, since the main purpose of this chapter is to determine the effect of the IR-UWB electromagnetic field on the SAR variations.

7.2.3 Temperature Variation Based on Bio Heat Model

When exposed to an electromagnetic field, the absorbed power by the body tissues causes a temperature increase. A temperature increase exceeding 1–2 °C in the human body tissue can cause adverse health effects, such as a heat stroke [43]. In addition to the study of SAR variations, this chapter also analyses the temperature variation in the human head when it is exposed to IR-UWB transmission from an implanted transmitter. The temperature of the body tissues is modelled using the bio heat equation in (7.10) [44]:

$$\mathrm{Cp}\frac{\delta \mathrm{T}}{\delta \mathrm{t}} = \nabla \cdot (\mathrm{k}\nabla \mathrm{T}) + \rho \cdot \mathrm{SAR} + \mathrm{A} - \mathrm{B}(\mathrm{T} - \mathrm{T_b}) \tag{7.10}$$

where K is the thermal conductivity, Cp denotes the specific heat, A is the basal metabolic rate, B is the term associated with blood perfusion, ρ is the tissue density in $\frac{\mathrm{kg}}{\mathrm{m}^3}$ and $\nabla \cdot (k\nabla T)$ represents the thermal spatial diffusion term for heat transfer through conduction at temperature T in degrees Celsius. The bio heat equation in (7.10) is solved with the boundary conditions given in (7.11), namely:

$$\mathrm{K}\frac{\delta \mathrm{T}}{\delta \mathrm{n}} = -\mathrm{h} \cdot (\mathrm{T} - \mathrm{T_a}) \tag{7.11}$$

where T_a is the temperature of the surrounding environment, n is the unit vector normal to the surface of interest and h is the convection coefficient for heat exchange with the external environment.

The human body tries to regulate its core temperature by various mechanisms in order to keep it at approximately 37 °C. The effect of thermo regulatory mechanisms causes the tissue specific basal metabolic rate (A) and blood perfusion

coefficient (B) in (7.10) to exhibit a dependency on body temperature rather than being a constant value. The basal metabolic rate is modelled using (7.12) [45]:

$$A = 1.1\, A_0^{T-T_0} \tag{7.12}$$

where T_o is the basal temperature and A_o is the basal metabolic rate of the tissue.

The blood perfusion is only dependent on the local blood temperature. Variation of the blood perfusion with the temperature is obtained using the set of equations presented in [46]. All the heat related parameters for the calculation of temperature variation are obtained from [46].

7.3 Case Study I: Electromagnetic Effects of IR-UWB Signals for Wireless Capsule Endoscopy Applications

WCE has many advantages over the traditional wired endoscopic methods. It does not require sedation of the patient or close monitoring of the procedure by a trained hospital staff. It can potentially be used for remote monitoring of the patients from isolated locations away from hospitals. One of the most important aspects of WCE is that it is the only method of obtaining images of the small intestine, whereas the wired endoscopy devices can only reach the colon or the upper part of the digestive tract [4, 47–50]. Many reported designs for wireless endoscopy system use a narrow-band wireless link in-order to transmit image data [4, 51]. However, compared to wired endoscopy methods, existing narrowband WCE devices suffer from limited battery life, low frame rate and low resolution [52]. IR-UWB can be identified as a wireless technology that can cater the demand for high data rate, low power consumption and small form factor requirement in the WCE devices [18, 53, 54]. Because of the increased interest in IR-UWB as a potential candidate for the wireless physical layer technology in WCE applications, it is important to analyze the electromagnetic effects caused by the pulse-based transmission on the human body. Figure 7.2 depicts a WCE system that uses IR-UWB for data communication.

7.3.1 Antenna Model and WCE Device Positioning

The simulations for WCE application use the UWB antenna model used in the simulations for the head implant application. It is tuned for better performance inside the abdomen of the human anatomical model. The antenna operates at a 4 GHz center frequency with a bandwidth of approximately 1 GHz. The 4 GHz center frequency is chosen to minimize the interference from other wireless technologies, such as 5 GHz Wi-Fi in a practical scenario. The dimensions of the

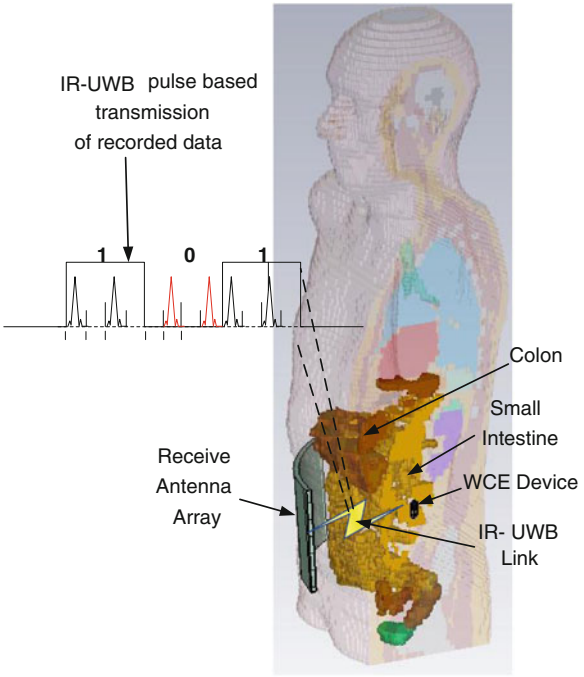

Fig. 7.2 IR-UWB based communication system for WCE

antenna model are 23.7 × 9 × 1.27 mm, which are comparable with the commercially available capsule sizes used for WCE [48]. The antenna is inserted in a capsule shaped case with a diameter of 9.5 mm. The thickness of the capsule walls is negligible compared to the dimensions of the antenna. The radiating element of the antenna used in the simulations, which occupies the lower half of the antenna, is inserted in glycerin-based gel for this purpose. Glycerin has a relative permittivity of 50, which is close to the relative permittivity of the surrounding tissue material; hence allows minimal reflections of the electromagnetic wave near the transitional boundaries between the tissue medium and the capsule.

The antenna is inserted inside the small intestine, at a distance of 89 mm from the front surface of the stomach, 88 mm from the left side of the stomach, and 645 mm from the top of the head as shown in Fig. 7.3. Initially, an FCC regulated IR-UWB pulse shown in Fig. 7.4 has been used as the excitation pulse in order to investigate SAR and temperature effects. The use of an FCC regulated UWB pulse for excitation is useful to compare the obtained results with the results available in the literature. Pulses with pulse duration of 2 ns are obtained from a pulse train with a period of 50 ns. A Band Pass Filter (BPF) is used to contain the pulse power within a bandwidth of 3.5–4.5 GHz. Initially, the pulse amplitude of the signal has been adjusted ensuring that the radiated power from the antenna falls within the FCC regulated power spectrum. The power calculation is done by integrating the power spectrum of the UWB pulse in the frequency range of 3.5–4.5 GHz using

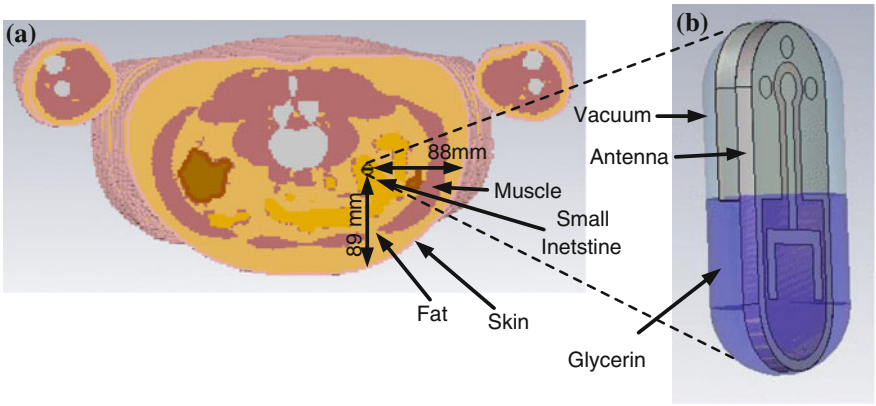

Fig. 7.3 **a** Top view simulated WCE device position **b** enlarged view of the WCE device

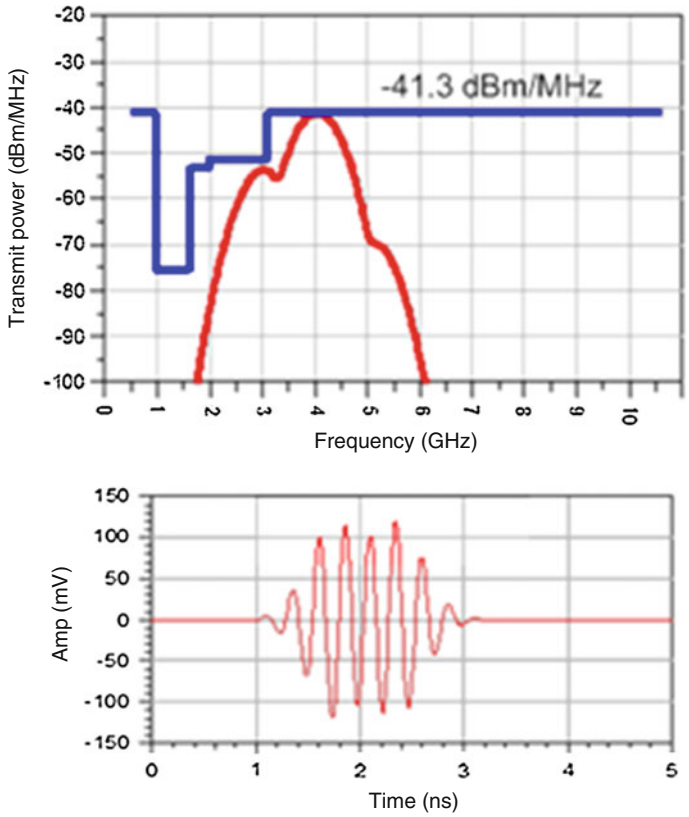

Fig. 7.4 The FCC regulated input pulse and its power spectrum

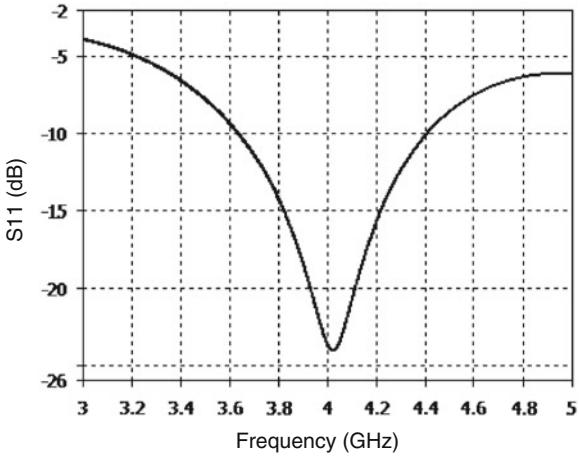

Fig. 7.5 Magnitude S-parameter plot for the implanted antenna position

the simulation software. Simulations recorded negative gain values for the antenna after tissue absorption; this means that the signal emitted in free space is lower than the radiated power from the implanted antenna. Hence, it is possible to excite the antenna with a signal power higher than the outdoor allowable 41.3 dBm/MHz power limit by increasing the excitation signal amplitude such that the power emitted to the free space after tissue absorption lies within the FCC regulations. Simulations are conducted in order to analyze the effect of this kind of manipulation on the SAR and temperature variation.

The S-parameters of the antenna for the above WCE position is depicted in Fig. 7.5. The two dimensional polar plot of the far field gain of the antenna at 4 GHz are shown in Fig. 7.6. The far field gain is shown on the x–y plane that passes through the centre of antenna. The angle (Phi) in Fig. 7.6 is measured in an anti-clockwise direction from the X-axis that passes through the centre of the antenna. The three dimensional far field antenna gain is calculated using (7.13), and converted into a two-dimensional plot using the gain values at the intersections with the x-y plane.

It can be seen from the far field results that the two-dimensional antenna gain is −63 dBi. It was observed from the simulations that the maximum three-dimensional gain is slightly higher than the two dimensional gain, and lies in the same direction. The gain is significantly low because of the large power absorption by the surrounding tissue mass. The recorded negative antenna gain after the tissue absorption means that a power level that is significantly higher than the FCC recommended spectral mask of −41.3 dBm/MHz for indoor transmission of the IR-UWB signals can be used for the antenna excitation, given that the regulations applied for SAR and SA are met [49, 50]. The delivered power to the antenna can be arranged such that the IR-UWB power level after the power loss due to tissue absorption lies within the FCC approved spectral mask. Simulations are carried out

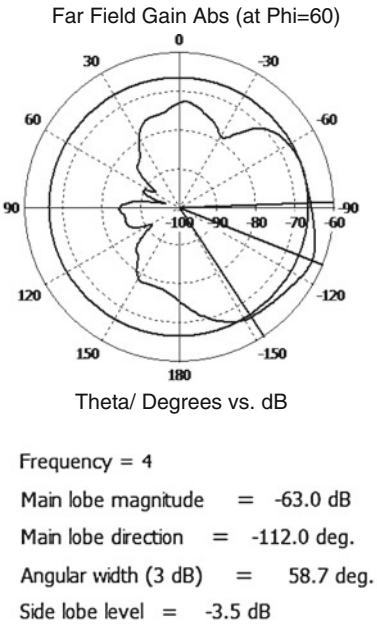

Fig. 7.6 Antenna far field gain plot at 4 GHz (Gain (dBi) vs. Phi (degrees))

using both the FCC regulated IR-UWB pulse and an IR-UWB pulse with a power spectrum that is higher than the FCC spectral mask in order to assess and compare the SAR variations.

7.3.2 SAR, SA Variations due to the Operation of IR-UWB-Based WCE Devices

SAR and temperature simulations are carried out for different signal power levels of the WCE antenna placed at a fixed position. Figure 7.7 presents the SAR variations for the first scenario. Figure 7.7a shows the SAR variation for an IR-UWB pulse with a total in-band signal power level which lies within the FCC spectral mask of −41.3 dBm/MHz. The SAR variation in Fig. 7.7b corresponds to an IR-UWB pulse that causes a maximum 10 g averaged SAR value of 2 W/kg which is the ICNIRP allowed SAR limit. Figure 7.7c depicts the SAR variation for an IR-UWB pulse that results in a signal power level just outside the human body to lay within the FCC regulated spectral mask. The maximum SA is calculated for each scenario using (7.9). An IR-UWB pulse width of 2 ns is used for the calculation of the SA. The in-band power of the IR-UWB pulses for the three different scenarios is varied by changing the pulse amplitude. The total in-band power for each simulation is calculated by integrating the power spectrum of the IR-UWB pulse in the frequency band of 3.5–4.5 GHz. The color scale in Fig. 7.7

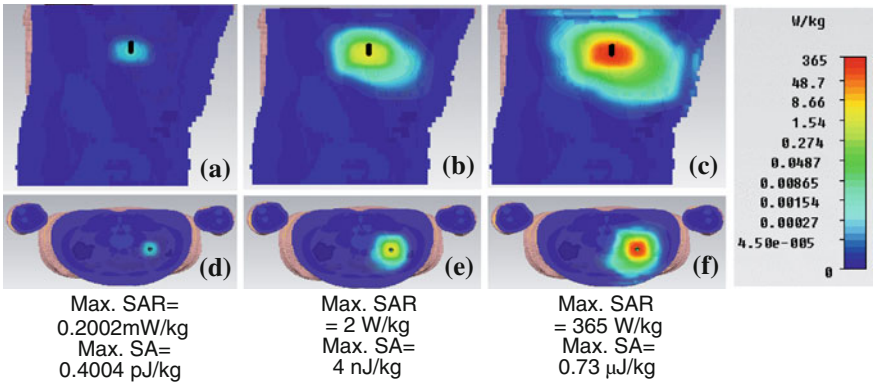

Fig. 7.7 Side view (**a**–**c**) and top view (**d**–**f**) of the simulated 10 average SAR variations in the human voxel model for IR-UWB pulses with peak spectral input power limits of (**a**–**d**) −41.3 dBm/MHz (**b**–**e**) −1.82 dBm/MHz (**c**–**f**) 21.7 dBm/MHz and total in-band signal power of (**a**–**d**) 0.0024 mW (**b**–**e**) 21.5 mW (**c**–**f**) 4.38 W

is set to reflect the maximum SAR in all the scenarios, and is logarithmically marked to yield an acceptable resolution for low SAR values.

The results depicted in Fig. 7.7 show that the SAR variation for the third scenario, where the input signal power is adjusted in order to obtain a signal with a power level that lies within the FCC allowed spectral mask just outside the body corresponds to an SAR variation that exceeds the ICNIRP allowed level of 2 W/kg. In other words, it can be observed from the results that it is the ICNIRP regulated SAR level of 2 W/kg that determines the maximum allowable signal power radiated from the antenna. This corresponds to an IR-UWB pulse with a total in-band signal power of 21.5 mW. The SAR variation shown in Fig. 7.7a is comparatively lower because of the small in-band power contained in the FCC regulated IR-UWB input pulse.

7.3.3 Temperature Variation Caused by IR-UWB-Based WCE Devices

The temperature variations for the same power level scenarios used for Fig. 7.7a–b are shown in Fig. 7.8. The temperature increase is obtained after the steady state is achieved. The initial body temperature is considered to be 37 °C. It can be observed from Fig. 7.8a that the temperature of the whole body has increased to 37.173 °C from the initial body temperature of 37 °C. There is no significant temperature increase in the tissues surrounding the WCE device compared to the tissues that are far away from it. This can be explained as follows: the temperature of the whole body has increased to 37.173°C due to the metabolic activities of the

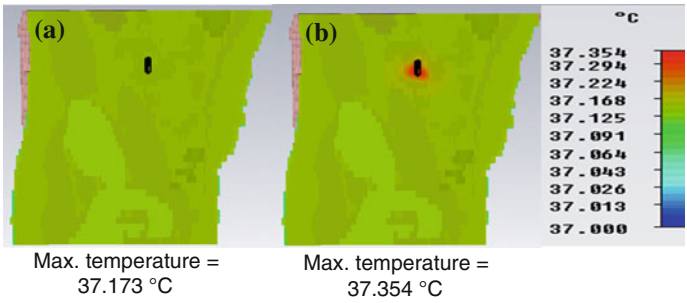

Fig. 7.8 Side view of the simulated temperature variation in the human voxel model for IR-UWB pulses with peak spectral input power limit of **a** −41.3 dBm/MHz with a total in-band signal power of 0.0024 mW **b** −1.82 dBm/MHz with a total in-band signal power 21.5 mW

Table. 7.2 SAR/SA comparison

Reference	Scenario	Body part	Reference input power	Frequency	MAX 10 g SAR/SA
[8]	In-body	Abdomen	25 mW	2.4 GHz	0.37 W/kg (SAR)
				1.2 GHz	0.64 W/kg (SAR)
				800 MHz	0.66 W/kg (SAR)
				430 MHz	0.62 W/kg (SAR)
				400 MHz	0.54 W/kg (SAR)
[22]	In-body	Abdomen	1 W (IR-UWB)	8.75 GHz	8.95 W/kg (SAR)
This study	In-body	Abdomen	−41.3 dBm/Mhz regulated IR-UWB	3.5–4.5 GHz	0.2 mW/kg (SAR) 0.4 pJ/kg (SA)
			21.5 mW (IR-UWB)		2 W/kg (SAR) 4 nJ/kg (SA)

body. The signal power of the FCC regulated delivered IR-UWB pulse is not enough to cause a significant temperature increase due to power absorption of the surrounding tissues. The blood perfusion in the human body is able to regulate the minute temperature increase caused by the small power absorption in this case. Meanwhile, the delivered pulse power for the simulations resulted in Fig. 7.8b is large enough to cause a temperature increase in the tissues at a close proximity to the WCE device. It can be observed that the temperature of the tissues at a close proximity to the WCE device has increased up to a maximum of 37.354 °C while rest of the tissues showed a temperature of 37.173 °C because of the metabolic activities. Table 7.2 compares the evaluated SAR values in this chapter with the related work in literature.

7.4 Case Study II: Electromagnetic Effects Caused by IR-UWB Signals Used in Head Implant Applications

This section presents the SAR/SA variation and temperature increase caused by IR-UWB signals used in head implant applications. This is compiled from the findings presented in [39, 51].

7.4.1 Head Implantable Antenna Model and Impedance Matching

A head implantable version of the antenna mentioned in above section is used for these simulations. The antenna is tuned to operate at around 4 GHz with a bandwidth of 1 GHz, which fulfils the bandwidth requirement imposed by the FCC for UWB communication. The antenna was inserted inside a capsule shaped casing with a negligible thickness compared to the antenna dimensions, in order to prevent direct contact between antenna radiating elements and the neighboring tissue. The radiating element of the antenna used in the simulations, which occupies the lower half of the antenna, is inserted in glycerin for the purpose of impedance matching. Glycerin has a relative permittivity of 50, which is close to the relative permittivity of the surrounding tissue material; hence allows minimal reflections of the electromagnetic wave near the transitional boundaries between the tissue medium and the capsule. The antenna is placed at 6 mm distance from the surface of the head. Figure 7.9 depicts how this antenna model is used alongside the CST voxel head model in order to perform present simulations. Through simulation-based optimization, the optimum value for the radius of the capsule ('D') was obtained to be 5 mm for the head implanted antenna, which is indicated in Fig. 7.9.

S-parameter characteristics and antenna gain/directivity far field characteristics are presented in Figs. 7.10 and 7.11, respectively. It should be noted that the near field characteristic of the antenna predominantly affects the SAR and the thermal behavior of the body tissues. The near field simulation characteristics are shown in the results section. Although the far field stretches outside of the brain and therefore does not influence the SAR, the far field characteristics are shown in order to compare the antenna performance in different scenarios as well as to get an idea about the direction in which the maximum power transfer is radiated by the antenna.

The three-dimensional far field antenna gain is calculated using the following equation:

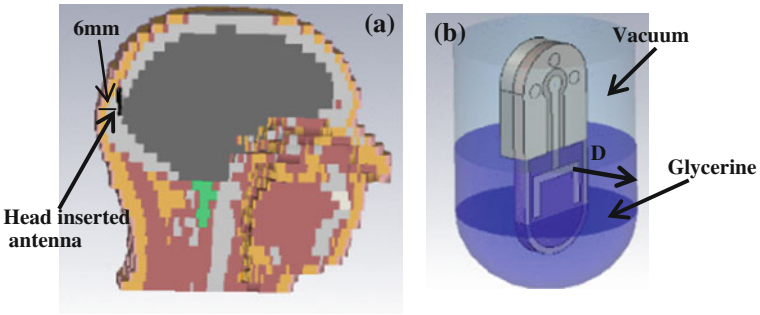

Fig. 7.9 **a** Insertion of the antenna in the head **b** IR-UWB implantable antenna

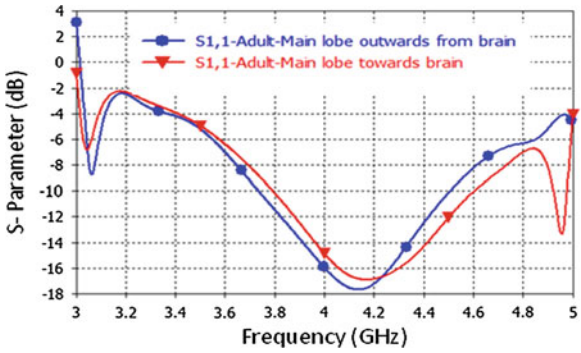

Fig. 7.10 Simulated S11 for the two different implant orientations, IEEE copyright [39]

$$G = 4\pi \cdot \frac{(P_{rad} - P_{tissue})}{P_i} \tag{7.13}$$

where G is the three dimensional gain, P_{rad} is the power radiated per unit solid angle, P_{tissue} is the power absorbed by tissues within the unit solid angle and P_i is the accepted power of the antenna after the antenna reflections. It should be noted that the antenna gain is high for antenna positions corresponding to low tissue absorptions.

7.4.2 SAR Variation for Different Signal Power Levels

10 g averaged SAR variations for three different signal power levels are analyzed for a 30-year-old adult head model using the developed simulation models (Fig. 7.11). The first scenario uses a FCC regulated IR-UWBIR-UWB pulse, which lies within the specified −41.3 dBm/MHz limit. The second scenario is obtained by considering the results in Fig. 7.11a, c: it can be observed in the latter

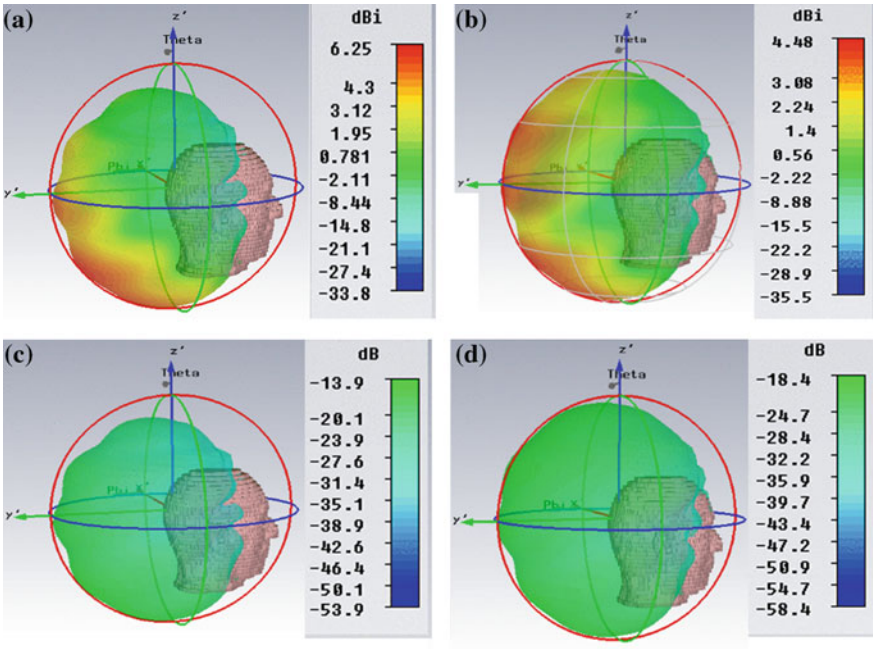

Fig. 7.11 **a–b** Directivity of the implanted antenna and **c–d** gain of the implanted antenna for (**a**, **c**) Antenna radiating outwards of the brain for adult head (**b**, **d**) Antenna radiating towards the brain for adult head

figure that the resulting maximum antennaAntenna gain is −13.9 dBi. This means that if a pulse with a peak power limit of 13.9 dB higher than the FCC regulated peak power limit of −41.3 dBm/MHz is used as the power from the implanted antenna, the radiation in free space will lie at the FCC limit. This corresponds to an input pulse with peak spectral limit of −27.4 dBm/MHz. In the third scenario, an IR-UWB pulse that causes a maximum SAR of 2 W/kg is used: the latter value is specified as the maximum allowable SAR limit by the ICNIRP regulations. The Specific Absorption (SA) in previous three scenarios is also calculated for a pulse width of 2 ns, in order to form a comparison with the ICNIRP special regulations for pulse transmissions. The results depicted in Fig. 7.12 show that the SAR and SA values obtained for the first and second scenario are well within the ICNIRP regulation limit for a single pulse of 2 W/kg and 2 mJ/kg respectively. This is due to the very small power contained in the signal (a total in-band accepted power of 0.0024 mW in scenario one and 0.0504 mW in scenario two considering a bandwidth of 1 GHz). It should be noted that the color scale is set to reflect the maximum SAR in all the scenarios, and is logarithmically marked to yield an acceptable resolution for low SAR values. The SAR variation in scenario three uses a signal which lies within a peak limit of 0.9 dBm/MHz for an amplitude

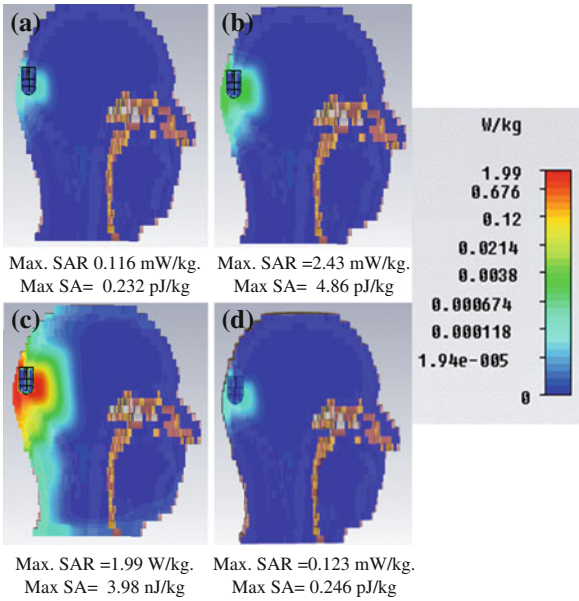

Fig. 7.12 Side view of the simulated 10 g averaged SAR variation in the adult voxel head model **a**–**c** when the antenna main lobe is situated outwards of the brain for the peak spectral power limits of **a** −41.3 dBm/MHz **b** −27.4 dBm/MHz and **c** 0.9 dBm/MHz **d** when the antenna main lobe is situated towards the brain for the peak spectral power limit of −41.3 dBm/MHz

increased version of the pulse shown in Fig. 7.4, but violates the FCC regulations for IR-UWB indoor propagation.

The effect of the antenna orientation is also considered in these simulations. Two cases are considered, depending on whether the main lobe is situated outwards or inwards of the brain. In the former case, the SAR variation is obtained by placing the antenna main lobe outwards of the brain for an adult head model aged at 30 years. In the latter case, the antenna main lobe radiates towards the brain. These two scenarios are used to represent various possible applications of wireless transmission in the head. For both cases, an FCC regulated IR-UWB pulse has been considered. The results obtained are shown in Fig. 7.12a, d. The SAR value for the adult head model with the antenna main lobe pointing towards the brain is 0.007 mW/kg higher than its counterpart shown in Fig. 7.12a. This is a comparatively negligible value and is caused by the different orientations in the near field.

7.4.3 SAR Variation in Different Tissue Materials in the Human Head

The SAR variation percentages for all the tissue types involved in the simulation of the IR-UWB signal with a peak power limit of −27.4 dBm/MHz and when the antenna main lobe is located outwards from the brain are shown in Fig. 7.13: this case corresponds to the simulation depicted in Fig. 7.12c. The mass percentage of each tissue type is indicated alongside the SAR. The total SAR recorded for this

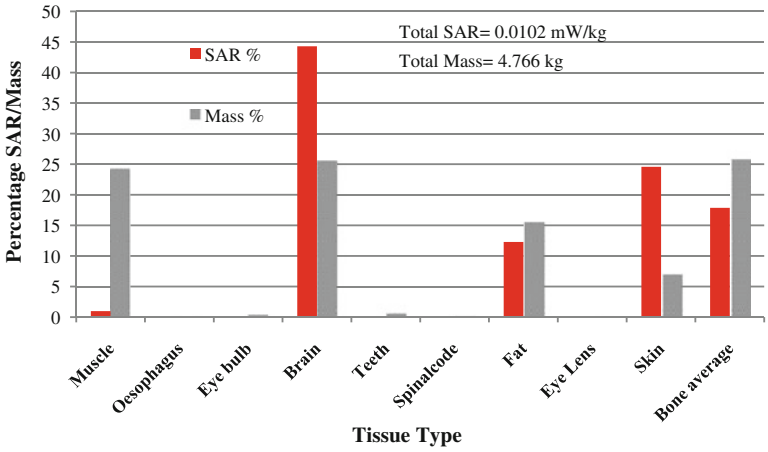

Fig. 7.13 SAR percentages and mass variation of tissue considered in the simulation, IEEE copyright [39]

scenario is 0.102 mW/kg, and the total mass of the head tissue is equal to 4.766 kg. It should be noted that the total SAR is calculated by dividing the total absorbed power by the corresponding tissue masses, unlike the calculation of the 10 g averaged SAR where local averaging over a 10 g of tissue material is considered and the maximal value is retained.

As illustrated in Fig. 7.13, brain, fat, skin and bone can be considered as tissue types with considerably high SAR percentage values. The maximum SAR percentages are recorded for the brain tissue. This is due to the fact that most of the radiated power from the antenna side lobe is directed towards the latter. The SAR percentage for the skin is relatively high considering its lower mass percentage; this is mainly due to the high water content in the former's tissue. The low water content in the bone tissue causes a comparatively low SAR value despite its comparatively high mass percentage.

7.4.4 Temperature Variation due to the Operation of IR-UWB-Based Head Implants

Simulations using the same input power scenarios as shown in Fig. 7.12a–c are used to obtain the corresponding temperature variations. The bio heat equation considers the variation of basal metabolic rate and blood perfusion. Because of the short duration of the excitation pulse, the heat conduction that occurs through sweating is assumed negligible. The temperature increase is obtained after the steady state is achieved. The initial body temperature is considered to be 37 °C. Figure 7.14 depicts the obtained temperature variations.

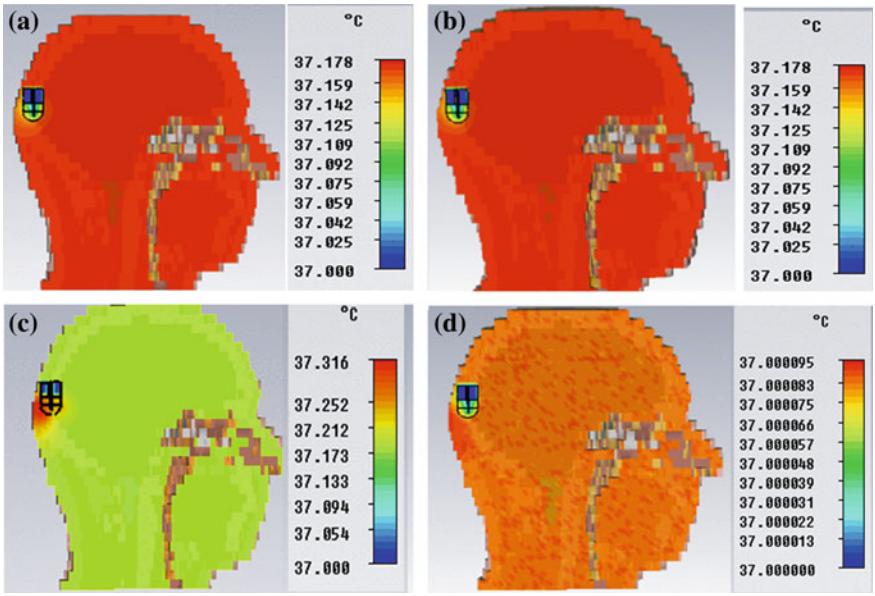

Fig. 7.14 Simulated temperature variation for a signal with peak spectral power limits of **a** −41.3 dBm/MHz **b** −27.4 dBm/MHz **c** 0.9 dBm/MHz using bio heat equation **d** −27.4 dBm/MHz without using bio heat equation, IEEE copyright [39]

It can be seen in Fig. 7.14a, b that the temperature of the whole head is increased from the initial temperature of 37–37.178 °C. It is not possible to see a significant temperature difference between the tissues at a close proximity to the antenna and those that are at a considerable distance from the antenna. This can be explained as follows. The temperature of the head as a whole increases up to 37.178 °C due to the metabolic activities in the tissues. The input powers to the antennas for cases shown in Fig. 7.14a, b are not large enough to cause a significant temperature increase due to the power absorption by the tissues. The temperature increases caused by the small radiated powers in these two cases are small enough to be regulated by the blood perfusion inside the head. This explanation is further justified by the results shown in Fig. 7.14c, d. The power delivered to the antenna for the case in Fig. 7.14c is higher than that of Fig. 7.14a, b. The high delivered power to the antenna generates a large enough electric field that causes high power absorption in the tissues. As a result, this high power absorption causes a considerable temperature increase in the tissues. It is clearly visible in Fig. 7.14c that the temperature of the tissues closer to the antenna are higher (a maximum of 37.316 °C is recorded in the simulations) than the temperature increase due to the metabolic activities in rest of the tissues (i.e. 37.178 °C). The simulations resulted in Fig. 7.14d ignore the heat generation from the metabolic activities and it does not regulate the temperature through blood perfusion. The power of the excitation pulse is set to fall within the −27.4 dBm/MHz spectral mask, which is similar to that of

Fig. 7.14b. There is an observed negligible temperature increase near the antenna for this case. This proves that the reason for the absence of a visible temperature increase for the simulations of Fig. 7.14b is blood perfusion. As can be observed in all four figures, the temperature in the glycerin insertion region of the antenna is lower than the temperature of the surrounding tissue that is heated up by metabolic activities. This is due to the fact that the initial temperature of glycerin is lower than the body temperature for the simulations.

7.5 Conclusion

IR-UWB has gained research interest as a lucrative wireless technology for wireless implant communication applications, such as WCE and neural recording systems. However, use of high frequency and wideband IR-UWB signals causes increased amount of electromagnetic power absorption by the human tissue. It is important to analyze these electromagnetic effects in order to assess the feasibility of using IR-UWB signals as a wireless implant communication technology. Unlike narrowband signals, IR-UWB signals are high frequency signals with a large bandwidth. Hence, characterizing the frequency dependent nature in the relative permittivity of the human tissue plays an important role in obtaining realistic results for electromagnetic effects caused by IR-UWB signals. This chapter describes the electromagnetic exposure effects caused by two types of UWB implanted devices used in wireless body area network applications: head implants and WCE devices. For the WCE applications of IR-UWB, it was observed that the SAR value determines the maximum IR-UWB transmit power that can be utilized in a WCE device that uses IR-UWB signals with 1 GHz bandwidth and a center frequency of 4 GHz. The maximum allowable total in-band power per pulse was found to be 21.5 mW for the particular WCE device position investigated in this chapter. The temperature increase caused by this transmit power level is discovered to be well within the control of thermal regulatory mechanisms of the human body.

For the head implant applications, the FCC regulations for the outdoor transmit power for UWB communication determines the maximum allowable signal power from an implanted IR-UWB based transmitter. It was observed for UWB based head implant applications that the SAR and SA results for the maximum peak power limit of −27.4 dBm/MHz falls within the ICNIRP regulated limits while emitting a UWB signal that falls within the FCC spectral mask when it propagates into the outdoor environment. The temperature increase due to the exposure of the head tissues to the IR-UWB electromagnetic field at those peak power limits is found to be well within the control of thermal regulatory mechanisms of the human body. Simulations also showed that it is possible to excite the antenna with a signal power higher than the outdoor allowable −41.3 dBm/MHz power limit. It was found that a pulse with a peak power limit of 13.9 dB higher than the FCC regulated peak power could be utilised for head implant applications of IR-UWB

without violating SAR/SA limits, as well as the outdoor FCC regulations for this particular model.

Acknowledgment The authors would like to thank Dr. Tharaka Dissanayake for his help in designing the UWB antenna used for the high frequency simulations. Also, special thank should be given to Monash e-Research Centre, Monash University, Australia for their cooperation in assisting this work by providing the high performance computing facility for the computationally intensive simulations.

References

1. N. Gopalsami, I. Osorio, S. Kulikov, S. Buyko, A. Martynov, A.C. Raptis, SAW Microsensor Brain Implant for Prediction and Monitoring of Seizures. IEEE Sens. J. **7**(7), 977–982 (2007)
2. A.V. Nurmikko, J.P. Donoghue, L.R. Hochberg, W.R. Patterson, Y.-K. Song, C.W. Bull, D.A. Borton, F. Laiwalla, S. Park, Y. Ming, J. Aceros, Listening to brain microcircuits for interfacing with external world. Proc. IEEE Prog. Wirel. Implantable Microelectron. Neuroeng. Devices **98**(3), 375–388 (2010)
3. C. Cavallotti, M. Piccigallo, E. Susilo, P. Valdastri, A. Menciassi, P. Dario, An integrated vision system with autofocus for wireless capsular endoscopy. Sens. Actuators, A **156**(1), 72–78 (2009)
4. X. Chen, X. Zhang, L. Zhang, X. Li, N. Qi, H. Jiang, Z. Wang, A wireless capsule endoscope system with low-Power controlling and processing ASIC. IEEE Trans. Biomed. Circ. Syst. **3**(1), 11–22 (2009)
5. ICNIRP, Guidelines for Limiting to time varying electric, magnetic, and electromagnetic fields (up to 300 GHz), in *International Commission on Non-ionizing Radiation Protection*, 1997
6. Institute of Electrical and Electronics Engineers (IEEE), in *IEEE Standard for Safety Levels with Respect to Human Exposure to Radio Frequency Electromagnetic Fields, 3 kHz to 300 GHz*. IEEE Std C95.1-2005 (2005)
7. P. Soontornpipit, Effects of radiation and SAR from wireless implanted medical devices on the human body. J. Med. Assoc. Thai. **95**(2), 189–197 (2012)
8. L. Xu, M.Q.H. Meng, H. Ren, Y. Chan, Radiation characteristics of ingestible wireless devices in human intestine following radio frequency exposure at 430, 800, 1200, and 2400 MHz. IEEE Trans. Antennas Propag. **57**(8), 2418–2428 (2009)
9. Q. Wang, J. Wang, SA/SAR analysis for multiple UWB pulse exposure, in *Asia-Pacific Symposium on Electromagnetic Compatibility and 19th International Zurich Symposium on Electromagnetic Compatibility*, pp. 212–215, 19–23 May 2008
10. M. Klemm, G. Troester, EM energy absorption in the human body tissues due to UWB antennas. Prog. Electromagnet. Res. **62**, 261–280 (2006)
11. V. De Santis, M. Feliziani, F. Maradei, Safety assessment of UWB radio systems for body area network by the FD2TD method. IEEE Trans. Magn. **46**(8), 3245–3248 (2010)
12. Z.N. Chen, A. Cai, T.S.P. See, X. Qing, M.Y.W. Chia, Small planar UWB antennas in proximity of the human head. IEEE Trans. Microw. Theor. Tech. **54**(4), 1846–1857 (2006)
13. C. Buccella, V. De Santis, M. Feliziani, Prediction of temperature increase in human eyes due to RF sources. IEEE Trans. Electromagn. Compat. **49**(4), 825–833 (2007)
14. N.I.M. Yusoff, S. Khatun, S.A. AlShehri, Characterization of absorption loss for UWB body tissue propagation model, in *IEEE 9th Malaysia International Conference on Communications*, pp. 254–258, 15–17 Dec 2009

15. A. Santorelli, M. Popovic, SAR distribution in microwave breast screening: results with TWTLTLA wideband antenna, in *Seventh International Conference on Intelligent Sensors, Sensor Networks and Information Processing*, pp. 11–16, 6–9 Dec 2011
16. F. Shahrokhi, K. Abdelhalim, D. Serletis, P.L. Carlen, R. Genov, The 128-channel fully differential digital integrated neural recording and stimulation interface. IEEE Trans. Biomed. Circuits Syst. **4**(3), 149–161 (2010)
17. M. Chae, Z. Yang, M.R. Yuce, L. Hoang, W. Liu, A 128-channel 6 mW wireless neural recording IC with spike feature extraction and UWB transmitter. IEEE Trans. Neural Syst. Rehabil. Eng. **17**, 312–321 (2009)
18. Y. Gao, Y. Zheng, S. Diao, W. Toh, C. Ang, M. Je, and C. Heng, Low-power ultra-wideband wireless telemetry transceiver for medical sensor applications. IEEE Trans. Biomed. Eng. **58**(3), 768, 772 (2011)
19. K.M.S. Thotahewa, A.I. AL-Kalbani, J.-M. Redoute, M.R. Yuce, *Electromagnetic Effects of Wireless Transmission for Neural Implants, Neural Computation, Neural Devices, and Neural Prosthesis* (Springer, New York, 2014)
20. O. Novak, C. Charles, R.B. Brown, A fully integrated 19 pJ/pulse UWB transmitter for biomedical applications implemented in 65 nm CMOS technology, in *2011 IEEE International Conference on Ultra-Wideband* (*ICUWB*), pp. 72–75, 14–16 Sept 2011
21. W.-N. Liu, T.-H. Lin, An energy-efficient ultra-wideband transmitter with an FIR pulse-shaping filter, in *International Symposium on VLSI Design, Automation, and Test*, pp. 1–4, 23–25 Apr 2012
22. T. Koike-Akino, SAR analysis in tissues for in vivo UWB body area networks, in *IEEE Global Telecommunications Conference*, pp. 1–6, 30 Nov–4 Dec 2009
23. P.J. Dimbylow, Fine resolution calculations of SAR in the human body for frequencies up to 3 GHz. Phys. Med. Biol. **47**(16), 2835–2846 (2002)
24. M.R. Basar, M.F.B.A. Malek, K.M. Juni, M.I.M. Saleh, M.S. Idris, L. Mohamed, N. Saudin, N.A. Mohd Affendi, A. Ali, The use of a human body model to determine the variation of path losses in the human body channel in wireless capsule endoscopy. Prog. Electromagnet. Res. **133**, 495–513 (2014)
25. D. Kurup, M. Scarpello, G. Vermeeren, W. Joseph, K. Dhaenens, F. Axisa, L. Martens, D. Vande Ginste, H. Rogier, J. Vanfleteren, In-body path loss models for implants in heterogeneous human tissues using implantable slot dipole conformal flexible antennas. EURASIP J. Wireless Commun. Netw. ISSN: 1687-1499 (2011)
26. A. Khaleghi, I. Balasingham, Improving in-body ultra wideband communication using near-field coupling of the implanted antenna. Microw. Opt. Technol. Lett. **51**(3), 585–589 (2009)
27. A. Khaleghi, R. Chávez-Santiago, I. Balasingham, Ultra-wideband statistical propagation channel model for implant sensors in the human chest. IET Microwaves Antennas Propag. **5**(15), 1805–1812 (2011)
28. CST Studio Suite™, CST AG, Germany, http://www.cst.com, 2014
29. FCC 02-48 (UWB First Report and Order), 2002
30. S. Gabriel, R.W. Lau, C. Gabriel, The dielectric properties of biological tissues: III. parametric models for the dielectric spectrum of tissues. Phys. Med. Biol. **41**(11), 2271–2293 (1996)
31. M. O'Halloran, M. Glavin, E. Jones, Frequency-dependent modelling of ultra-wideband pulses in human tissue for biomedical applications, in *IET Irish Signals and Systems* Conference, pp. 297–301 (2006)
32. S.C. DeMarco, G. Lazzi, W. Liu, J.D. Weiland, M.S. Humayun, Computed SAR and thermal elevation in a 0.25-mm 2-D model of the human eye and head in response to an implanted retinal stimulator—part I: models and methods. IEEE Trans. Antennas Propag. **51**(9), 2274–2285 (2003)
33. C. Gabriel, S. Gabriel, R.W. Lau, The dielectric properties of biological tissues: I. Literature survey. Phys. Med. Biol. **41**(11), 2231–2249 (1996)

34. A. Peyman, C. Gabriel, E.H. Grant, G. Vermeeren, L. Martens, Variation of the dielectric properties of tissues with age: the effect on the values of SAR in children when exposed to walkie–talkie devices. Phys. Med. Biol. **54**(2), 227–241 (2009)
35. C. Gabriel, Dielectric properties of biological tissue: variation with age. Bioelectromagnetics, **26**(7), 12–18 (2005)
36. J. Wang, O. Fujiwara, S. Watanabe, Approximation of aging effect on dielectric tissue properties for SAR assessment of mobile telephones. IEEE Trans. Electromagn. Compat. **48**(2), 408–413 (2006)
37. K. Lichtenecker, Die dielektrizitatskonstante naturlicher und kunstlicher mischkorper. Phys. Z. **27**, 115–158 (1926)
38. P.L. Altman, D.S. Dittmer, *Biology Data Book: Blood and Other Body Fluids* (Federation of American Societies for Experimental Biology, Washington, DC, 1974)
39. K.M.S. Thotahewa, J.M. Redoute, M.R. Yuce, SAR, SA, and temperature variation in the human head caused by IR-UWB implants operating at 4 GHz. IEEE Trans. Microw. Theory Tech. **61**, 2161–2169 (2013)
40. T. Weiland, M. Timm, I. Munteanu, A practical guide to 3-D simulation. IEEE Microwave Mag. **9**(6), 62–75 (2008)
41. M. Clement, T. Weiland, Discrete electromagnetism with finite integral technique. Prog. Electromagn. Res. **32**, 65–87 (2001)
42. IEEE C95.3-2002, Recommended practice for measurements and computations of radio frequency electromagnetic fields with respect to human exposure to such fields, 100 kHz–300 GHz, in *IEEE Standard C95.3*, 2002
43. ACGIH, Threshold limit values for chemical substances and physical agents and biological exposure indices, in *American Conference of Governmental Industrial Hygienists*, 1996
44. H.H. Pennes, Analysis of tissue and arterial blood temperatures in resting forearm. J. Appl. Physiol. **1**, 93–122 (1948)
45. M. Hoque, O.P. Gandhi, Temperature distributions in the human leg for VLF-VHF exposures at the ANSI recommended safety levels. IEEE Trans. Biomed. Eng. **35**, 442–449 (1988)
46. P. Bernardi, M. Cavagnaro, S. Pisa, E. Piuzzi, Specific absorption rate and temperature elevation in a subject exposed in the far-field of radio-frequency sources operating in the 10–900-MHz range. IEEE Trans. Biomed. Eng. **50**(3), 295–304 (2003)
47. S.H. Lee, J. Lee, Y.J. Yoon, S. Park, C. Cheon, K. Kim, S. Nam, A wideband spiral antenna for ingestible capsule endoscope systems: experimental results in a human phantom and a pig. IEEE Trans. Biomed. Eng. **58**(6), 1734–1741 (2011)
48. A. Moglia, A. Menciassi, M.O. Schurr, P. Dario, Wireless capsule endoscopy: from diagnostic devices to multipurpose robotic systems. Biomed. Microdevices **9**(2), 235–243 (2007)
49. T. Dissanayake, K.P. Esselle, M.R. Yuce, Dielectric loaded impedance matching for wideband implanted antennas. IEEE Trans. Microw. Theory Tech. **57**(10), 2480–2487 (2009)
50. K.M.S. Thotahewa, J.M. Redoute, M.R. Yuce, Electromagnetic power absorption of the human abdomen from IR-UWB based wireless capsule endoscopy devices, in *IEEE International Conference on Ultra-Wideband (ICUWB)*, pp. 79–84, 2013
51. K.M.S. Thotahewa, J.-M. Redoute, M.R. Yuce, Electromagnetic and thermal effects of IR-UWB wireless implant systems on the human head, in *35th Annual International Conference of the IEEE Engineering in Medicine and Biology Society* (*EMBC*), pp. 5179–5182, Osaka, Japan, Jul 2013
52. G. Pan, L. Wang, Swallowable wireless capsule endoscopy: Progress and technical challenges. Gastroenterol. Res. Pract. **2012** (841691), 9 (2012)
53. M.R. Yuce, T. Dissanayake, Easy-to-swallow wireless telemetry. IEEE Microw. Mag. **13**, 90–101 (2012)
54. C. Kim, S. Nooshabadi, Design of a tunable all-digital UWB pulse generator CMOS chip for wireless endoscope. IEEE Trans. on Bio-Med. Circuits Syst. **4**(2), 118–124 (2010)